JOURNAL OF GEOPHYSICAL RESEARCH, VOL. 113, C08030, doi:10.1029/2007JC004550, 2008



# Estimates of surface roughness length in heterogeneous under-ice boundary layers

W. J. Shaw,[1] T. P. Stanton,[1] M. G. McPhee,[2] and T. Kikuchi[3]

Received 11 September 2007; revised 19 February 2008; accepted 30 May 2008; published 19 August 2008.

[1] Measurements obtained in the under-ice ocean boundary layer by two autonomous buoys deployed in 2004 and 2005 are used to estimate the roughness length $z_0$ of the underside morphology of Arctic Ocean pack ice. Two techniques are used to estimate $z_0$. The first uses an extension of the law of the wall and directly measured turbulent shear stress and velocity at a single point near the ice-ocean interface. The second uses a one-dimensional numerical boundary layer model that is matched to measured velocity profiles in the outer part of the boundary layer with $z_0$ as an adjustable parameter. The stress-based estimates are sensitive to local morphological features, and the effect of nearby ice ridge keels on the roughness estimates is evident. Averaged over flow direction there is a significant difference in floe roughness between the 2004 and 2005 deployments. Velocity-profile-based $z_0$ estimates are more uniform with direction than the stress-based estimates, and the average value of the profile-based estimates lies within the range of the stress-based estimates. Averaged over flow direction, both techniques yield $z_0$ estimates of about 100 mm for the 2005 data set. A central question is how to best estimate a $z_0$ that can be applied to an individual grid cell in large-scale numerical models. The profile-based estimates are promising in this regard because they are less affected by local morphology than stress-based measurements, which must be made fairly close to the interface in order to be interpretable using a framework based on the law of the wall.

**Citation:** Shaw, W. J., T. P. Stanton, M. G. McPhee, and T. Kikuchi (2008), Estimates of surface roughness length in heterogeneous under-ice boundary layers, *J. Geophys. Res.*, *113*, C08030, doi:10.1029/2007JC004550.

## 1. Introduction

[2] The shear stress between pack ice and the upper ocean, largely supported by turbulent flow in the under-ice ocean boundary layer (IOBL), is an important component of high-latitude, air/ice/ocean interaction because it is the mechanism by which momentum is transferred between ocean and ice and because ocean/ice exchange rates of heat and salt (or any other quantity of interest, for that matter) are modulated by its magnitude. The amount of drag between ice and ocean is affected by the morphology of the underside of the ice, so surface roughness estimates are needed to calculate the ice/ocean interface shear stress. For a given ice speed, rough pack ice will generate larger amplitude shear stress in the IOBL (and larger ocean/ice exchange rates) than smooth ice. For the IOBL, it is difficult to estimate spatially representative values of surface roughness owing to the extreme heterogeneity of the ice underside morphology. In this paper we explore two techniques for estimating surface roughness in the Arctic IOBL using long-duration data sets from two ice-tethered, observing systems that we call autonomous ocean flux buoys (AOFBs).

[3] Rossby similarity theory [e.g., *Blackadar and Tennekes*, 1968] provides a quantitative framework for describing drag relationships in planetary boundary layers including the IOBL [*McPhee*, 1990]. Although Rossby similarity was developed in the context of a geostrophic flow over a stationary boundary (i.e., the atmospheric boundary layer), it applies directly to the case of an ocean surface boundary layer forced by a surface stress in a relative coordinate system that moves at the surface velocity [e.g., *Tennekes and Lumley*, 1972]. The theory assumes that the boundary layer is horizontally homogeneous and neutrally stratified, and it is based on a dimensional analysis of dynamically significant boundary layer length scales:

$$\text{surface roughness length} : z_0$$
$$\text{distance from the interface} : z$$
$$\text{Ekman boundary layer depth scale} : d_E = \frac{|\mathbf{u}_{*\mathbf{0}}|}{f}$$

The roughness length $z_0$ parameterizes the hydrodynamic effect of the interface morphology on the boundary layer flow. The depth-limiting effect of planetary rotation on the boundary layer is represented by the Ekman scale $d_E$ where $f$ is the Coriolis parameter and $\mathbf{u}_{*\mathbf{0}}$ is the interface friction velocity defined by $\mathbf{u}_{*\mathbf{0}} = \boldsymbol{\tau}_0/\rho$, in which $\boldsymbol{\tau}_0$ is the interface

[1] Oceanography Department, Naval Postgraduate School, Monterey, California, USA.
[2] McPhee Research Company, Naches, Washington, USA.
[3] Japan Marine Science and Technology Center, Yokosuka, Japan.


0148-0227/08/2007JC004550$09.00

shear stress. (Throughout the remainder, boldface notation is used to indicate horizontal vectors.) These three scales interact (in a manner described further in section 4.2) to determine the turbulent length scale. Useful results of the theory are obtained by matching velocity profiles (nondimensionalized by $\mathbf{u}_{*\mathbf{0}}$) corresponding to the inner layer, where the $d_E$ has no dynamic effect, and the outer layer, where $z_0$ has no dynamic effect. For the ocean surface layer case, inner layer currents relative to the surface velocity are self-similar as a function of the normalized coordinate $z/z_0$, and the absolute outer layer currents are self-similar as a function of the normalized coordinate

$$\eta = \frac{z}{d_E} = \frac{fz}{u_{*0}} \tag{1}$$

referred to hereafter as the scaled depth.

[4] Close, but not too close, to the interface, the classical law of the wall,

$$\frac{\mathbf{U}}{\mathbf{u}_{*\mathbf{0}}} = \frac{1}{\kappa}\ln\frac{z}{z_0}, \tag{2}$$

holds in the overlap/log layer, where the inner and outer layer solutions are matched. Within the log layer, $z$ is the only significant length scale and stress is approximately equal to the interface value. Here, $\mathbf{U}$ is the vector horizontal fluid velocity relative to the moving ice as a function of $z$ and $\kappa$ is von Karman's constant (taken as 0.41). Within the log layer, velocity and shear stress are aligned and the stress is approximately constant. The vertical extent of the log layer is constrained by the conditions $z/z_0 \gg 1$ and $\eta \ll 1$, to ensure that $z$ is the only relevant length scale; in practice, the log layer is confined approximately to $\eta < 0.05$, excluding the roughness sublayer, $z/z_0 \sim 1$, that is directly affected by the surface morphology.

[5] From an observational perspective, (2) is useful because it allows estimation of $z_0$ from point measurements of $\mathbf{U}_m$ and $\mathbf{u}_{*m}$ at an elevation $z_m$ within the log/constant stress layer. The dimensionless velocity

$$\boldsymbol{\nu}_m = \frac{\mathbf{U_m}}{\mathbf{u_{*m}}} \tag{3}$$

is the inverse square root of a local drag coefficient and it is simply related to $z_0$

$$\nu_m = \frac{U_m}{u_{*m}} = \frac{1}{\kappa}\ln\frac{z_m}{z_0}, \tag{4}$$

providing a standard technique for estimating $z_0$ in many types of boundary layers, the IOBL included [e.g., *McPhee*, 2002].

[6] A second result of the matching of inner and outer layer velocity profiles is an inverse geostrophic drag law that relates the relative speed at the outer edge of the boundary layer to $\mathbf{u}_{*0}$

$$\boldsymbol{\Gamma} = \frac{\mathbf{V_0}}{\mathbf{u}_{*\mathbf{0}}} = \frac{1}{\kappa}\left(\ln\frac{u_{*0}}{fz_0} - A + iB\right). \tag{5}$$

$\mathbf{V_0}$ is the ice (surface) velocity with respect to undisturbed geostrophic flow in the ocean, i.e., the current that would exist in the absence of boundary layer forcing. In practice, it is often taken to be the measured ice velocity, since geostrophic flow is typically small compared with wind-driven drift velocity. A and B are similarity constants. The geostrophic drag coefficient is a function of the friction Rossby number

$$\mathrm{Ro}_* = \frac{u_{*0}}{fz_0},$$

the ratio of boundary layer scale height $d_E$ to roughness length. Note that although the scaled absolute currents in the outer layer are $z_0$-independent, the angle between the surface stress and the deep relative currents is $z_0$-dependent because the relative velocity at the outer edge of the log layer is a function of $z_0$ as indicated by (2).

[7] From a modeling perspective, Rossby similarity (5) is useful because it provides a prescription for calculating the interface shear stress given ice speed and an estimate of the surface roughness. It is customary to express the magnitude of interfacial stress as a power law. Most pack ice and ice/ocean interaction models use a quadratic stress law, i.e power law exponent $n = 2$ [e.g., *Hibler*, 1979]. However, according to (5), the nondimensional surface velocity is not constant but depends on both $z_0$ and $u_{*0}$. Indeed, results from the year-long AIDJEX drift stations in 1975–1976, showed that the exponent in the stress/velocity power law was close to 1.7 instead of 2, consistent with Rossby similarity [*McPhee*, 1979]. If $z_0$ can be estimated, (5) provides a better physical representation of under-ice drag than a constant coefficient, quadratic drag law. Potential applications of (5) include use as the surface boundary condition in large-scale numerical models and calculation of ocean-to-ice heat flux. For example, hundreds of position-reporting buoys have been deployed in the Arctic pack ice (see, e.g., http://iabp.apl.washington.edu); again if $z_0$ can be estimated, (5) can be used to calculate $\mathbf{u}_{*\mathbf{0}}$ along buoy drift tracks using position-record-derived ice velocities $\mathbf{V_0}$. When mixed layer temperature departure from freezing is also measured accurately, the two records can be combined to produce ocean-to-ice heat flux estimates [*McPhee et al.*, 2003; *Krishfield and Perovich*, 2005].

[8] The basic assumptions of Rossby similarity (horizontal homogeneity and neutral stratification) are, however, often not satisfied in the IOBL, limiting the direct application of (2) and (5) in observational or modeling studies. The most immediate problem encountered when attempting to estimate the hydraulic roughness of the underside of pack ice is the large variability of the interface morphology: very rough in the vicinity of pressure ridge keels to very smooth near newly refrozen leads [*Wadhams*, 1988; *Wadhams et al.*, 2006]. For example, measurements of Reynolds stress made relatively near the ice/ocean interface are often sensitive to the direction of flow with respect to upstream roughness elements [*McPhee*, 2002, 2008]. A long acknowledged problem with inferring general air/ice/ocean exchanges from limited measurements is gauging how representative those measurements are of the entire floe or surrounding region: the scaling up problem. For practical reasons, subice instruments are usually placed below relatively smooth ice,

away from obvious obstacles. Consequently, measurements made near the interface often sense roughness over a limited upstream fetch, and thus do not represent well overall floe roughness. We also often find that Reynolds stress increases with distance from the interface as the longer upstream fetch sensed by the instruments encompasses larger roughness elements [*McPhee*, 2002]. An obvious solution to the problem of heterogeneous ice bottom morphology is to estimate $z_0$ using measurements made as far away from the interface as possible. Measurements made far from the boundary will have a larger upstream fetch or flux footprint [*Horst and Weil*, 1992] than measurements made close to the boundary, and will therefore tend to be more spatially representative. Relatively deep measurements also provide better scale separation between $z$ and $z_0$, which may be a restriction when under-ice roughness elements are particularly large. In extreme cases, for example a large pressure ridge keel plowing through a shallow surface mixed layer, $z_0$ and $h_E$ are comparable and the whole concept of an overlap/log layer should be discarded [*Jimenez*, 2004]. Of course, basing roughness estimates on measurements obtained relatively far from the interface introduces other complexities that we address with two different approaches.

[9] The law of the wall (2) provides a straightforward technique to estimate $z_0$. The desire to attain spatial representativeness by using measurements far from the boundary conflicts, however, with the requirement of the law of the wall for the scaled measurement height $\eta$ to be small. For the IOBL, the vertical extent of the log layer is typically not more than a few meters. This is in contrast to the much thicker atmospheric surface boundary layer, where the log layer is often instrumented with vertical arrays up to hundreds of meters in extent. If surface buoyancy forces are significant, for example, during conditions of rapid ice melting, the vertical extent is reduced further. To resolve this conflict, we use an extension of the law of the wall that allows application deeper into the boundary layer.

[10] As indicated by the geostrophic drag law (5), the turning of relative outer boundary layer currents is a function of $z_0$ and provides the basis for the second technique for estimating roughness. If $\mathbf{V_0}$ and $\mathbf{u_{*0}}$ can be accurately determined, (5) provides a direct estimate of $z_0$. The problems with this approach are first that stratification often significantly affects outer layer currents and second that the difficulty of estimating a spatially representative $\mathbf{u_{*0}}$ remains. From the perspective of Rossby similarity, the effect of stratification on the boundary layer is to introduce additional length scales, such as the Monin-Obukhov length for buoyancy fluxes within the boundary layer, or a mixed layer depth scale that inhibits boundary layer growth because of stratification near the bottom of the well-mixed layer. When stratification is significant, the similarity constants $A$ and $B$ become stratification-dependent similarity functions. Still, exploiting the turning angle of relative outer layer currents is attractive, so we employ a new technique described by *McPhee* [2008] that matches observed outer boundary layer current profiles to those in a one-dimensional numerical boundary layer model with adjustable $z_0$. The technique does not require estimates of $\mathbf{u_{*0}}$ and it explicitly accounts for stratification effects in the outer part of the boundary layer.

[11] In this paper, we use measurements of Reynolds shear stress and currents in the IOBL from two, 1-year-long AOFB deployments to estimate the variability of surface roughness estimates associated with the two ice floes: one was fairly homogeneous and the other was bordered on two sides by large ice ridges. The data sets used are interesting and unique because of the contrast in the under-ice morphology of the two case studies and because the long duration of the measurements allows a high level of confidence in the derived statistics. Roughness length is investigated using the two approaches described above with the goal of obtaining spatially representative roughness estimates. In particular, the underside morphology of the small floe with ridges must have been fairly simple because stress-based estimates of roughness length were clearly larger for flow direction perpendicular to the ridges than for flow directions parallel to the ridges. The velocity-model-based roughness estimates are more uniform with direction, indicating that they are representative of a larger spatial area.

## 2. Autonomous Ocean Flux Buoys

[12] The autonomous ocean flux buoy (AOFB) is a system for measuring turbulent fluxes in the upper ocean below sea ice that is custom designed and fabricated within the Ocean Turbulence Group at the Naval Postgraduate School (NPS). The AOFBs (Figure 1 and see also http://www.oc.nps.navy.mil/stanton/fluxbuoy) have two main components: a surface buoy that sits on the ice and an instrument frame that is suspended into the upper ocean by a series of torsionally rigid poles from the bottom of the surface buoy.

[13] The surface buoy contains processing electronics, Global Positioning System (GPS) electronics, an Iridium satellite modem, GPS and Iridium antennae, and batteries. The instrument frame is outfitted with a downward looking 300 kHz Acoustic Doppler Current Profiler (ADCP, RDI Workhorse) and a custom-built flux package. After installation in the field on selected ice floes, AOFBs maintain twice-daily, two-way communications with a computer running at NPS. During each data transfer, sampling parameters may be updated.

[14] An NPS-calibrated acoustic traveltime current meter (Falmouth Scientific Inc., ACM 3D current meter, 1.5 mm $s^{-1}$ r.m.s. noise level), an inductive conductivity cell ($\pm 0.002$ mS $cm^{-1}$) and platinum resistance thermometer (Falmouth Scientific Inc., OEM C-T Sensor), and a fast response thermistor ($\pm 1$ mC) comprise the suite of sensors on the flux package. These fast response sensors are collocated within a 0.001-$m^3$ sample volume and are designed to directly measure the turbulent fluxes of momentum, heat, and salt using the eddy correlation technique and are burst-sampled over approximately 20-min-long Reynolds averaging periods. For each averaging period, first- and second-order statistics are calculated onboard the buoy for velocity, temperature, and salt, including the covariance of vertical velocity with horizontal velocity, temperature, and salinity (i.e., the vertical turbulent fluxes of momentum, heat and salt). In particular, the kinematic turbulent shear stress, and hence the friction velocity is

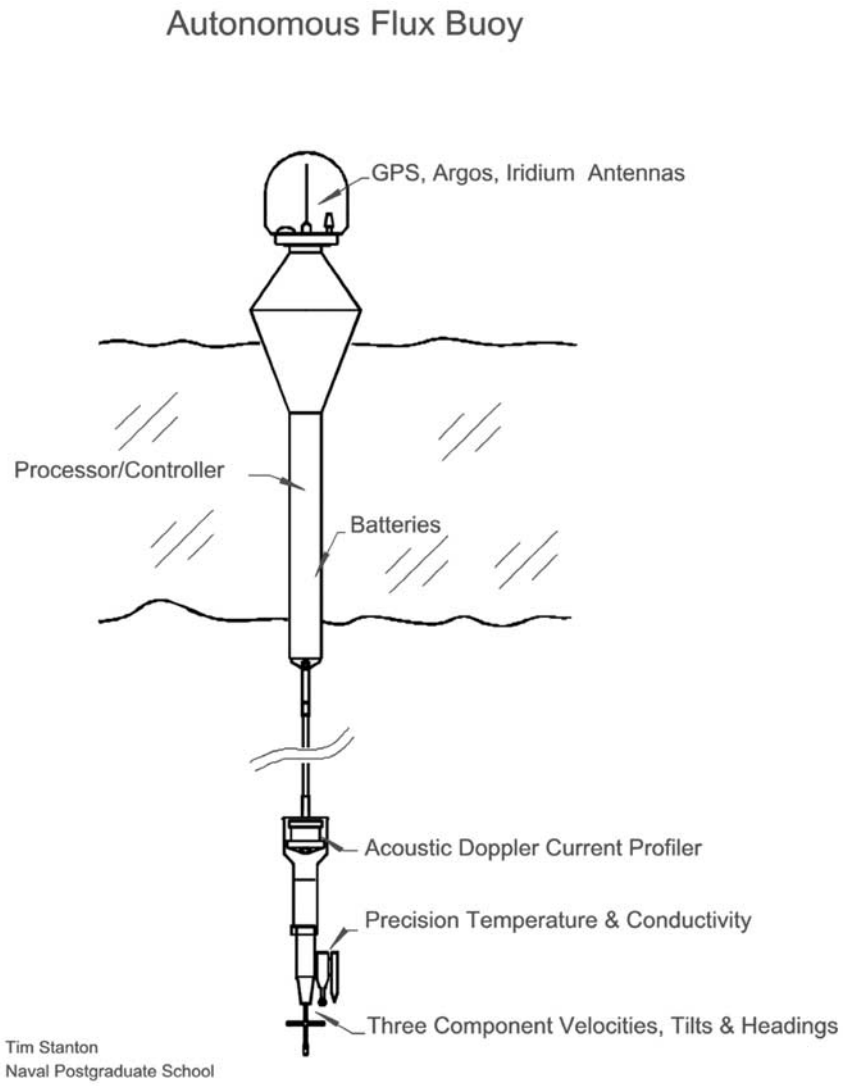


**Figure 1.** Diagram of an autonomous ocean flux buoy. The buoy housing rests on the surface of the ice from which the instrument frame with flux package and ADCP is suspended into the IOBL.

directly measured by the correlation of the fluctuating horizontal and vertical velocity components,

$$\boldsymbol{\tau}/\rho = u_* \mathbf{u}_* = \overline{\mathbf{u}' w'}, \tag{6}$$

where the overbar notation indicates Reynolds averaging over the sample periods and the prime notation indicates fluctuations about the average. Estimates of friction speed calculated from the eddy correlation stress have a noise level of about 0.002 m $s^{-1}$ in $u_{*m}$. In addition to the first and second moments from the Reynolds averaging periods, spectra and cospectra of fluctuating quantities, including the vertical velocity, are calculated onboard the buoy and are included in the data transmissions.

[15] The setups of the sensors on the two buoys described here were essentially identical. The first velocity bin of the ADCP profile is located 8.9 m below the surface of the ice, the vertical bin size is 2 m, and 40 depth bins are recorded. The sampling volume of the flux package instruments is located 7.6 m below the surface of the ice. The more dynamically relevant measure, distance from the bottom of the interface $z$, varies with ice thickness obviously, which is typically 2–2.5 m for the floes on which the buoys have been deployed. The flux package measurement depth of 5 m below the ocean-ice interface was chosen as a compromise between having a large fetch for the flux estimates and having an acceptable amount of flux attenuation at the measurement depth compared to values at the interface (i.e., for momentum flux, the sensor should be in the approximately constant stress layer). These statements are quantified in section 4.

[16] The autonomous aspect of the deployments limits the power budget onboard the buoys and prohibits continuous, rapid sampling of the sensors. Instead, the instruments are periodically burst-sampled at high frequency. The sampling strategies used to create the two data sets used here were very similar: instruments recorded data over the initial 40 min of a 4-h-long sampling interval. At the beginning of each 4-h interval, the flux package sensors sampled for two 18-min-long, Reynolds-averaging periods at a sample

rate of 3.8 Hz. Over the same time period, the ADCP took either three or four 10-min-averaged vertical velocity profiles or six or seven 5-min-averaged velocity profiles.

[17] A shortcoming of the traveltime current meter used in the flux package is a tendency for the zeros of its along-path velocities to drift over time and with changes in temperature. Owing to the instrument's geometry, one of the four acoustic paths always lies in the wake of a central, structural element. A path-switching algorithm is used to construct the velocity vector from the three undisturbed paths. Problems arise when there are many path switches over a Reynolds averaging period and the path zeros are not accurately known. The combination of inaccurate zero offsets and frequent path switching contaminates flux estimates by making false contributions to the fluctuating quantities. The magnitude of the variability of the zero offset drifts was not initially recognized and was not fully accounted for in the onboard processing for the two buoy data sets considered here, although the number of switching events for each averaging period was reported. Plots of Reynolds stress estimates as a function of number of switches (not shown) indicate that the stress estimates were degraded by the path switching when a threshold value of about 30 switches in an averaging period was exceeded. To avoid these contaminations, Reynolds averaging periods that contained more than 30 path switches are excluded from the analysis. Frequent path switching occurs when the flow is aligned with one of the instrument coordinate horizontal axes. As a result there are significant data gaps for flows oriented at 0°, 90°, 180°, and 270° in the current meter instrument coordinate system.

[18] For analysis purposes, all the buoy data (flux package sensors, ADCP, and GPS) are averaged over the 40-min-long sampling interval, resulting in a time series with nominal 4-h spacing. Over this period of time, the error in GPS-derived ice velocity estimates is less than 7 mm $s^{-1}$. This averaging period is not long compared to the timescales of flux-carrying eddies in the IOBL (about 10 minutes for moderate forcing at the measurement height of the flux package) and so it is to be expected that the resulting stress estimates will contain a large amount of random variation. Our strategy for dealing with this measurement variability is to consider heavily averaged forms of the data. The instrument coordinate system of the current meters provides a natural reference frame to look at directional aspects of the data sets because it is approximately fixed with respect to the morphological features of the ice underside. Furthermore, because of the data gaps in the directions of the traveltime current meter instrument coordinate system that result from the path switching problem described above, a convenient way to separate data by flow orientation is by quadrant of the horizontal angle measured by the traveltime current meter.

## 3. North Pole Environmental Observatory Deployments

[19] On a continuing basis started in 2002, AOFBs have collected upper ocean measurements in the Eastern Arctic Ocean following springtime deployments at the North Pole Environmental Observatory (NPEO) ice camps (see http://psc.apl.washington.edu/northpole for more information about the NPEO program). Over the course of a year or so, the buoys collect data as the Transpolar Drift carries them southward. Data collection ends when the buoys melt out of the ice and the systems are eventually damaged by surface wave motion. To date, this has occurred after the buoys have passed through Fram Strait into the Greenland Sea. At the NPEO camps, the AOFBs were collocated on the same floe with other autonomous measuring systems: National Ocean and Atmospheric Administration Pacific Marine Environmental Laboratory (PMEL) meteorological installations (http://www.arctic.noaa.gov/gallery_np.html), U.S. Army Cold Regions Research and Engineering Laboratory (CRREL) ice mass balance buoys (http://www.crrel.usace.army.mil/sid/IMB/index.htm), Japan Agency for Marine-Earth Science and Technology Compact Arctic Drifter (JCAD, http://www.jamstec.go.jp/arctic/index_2e.htm) which measures temperature and salinity at discrete depths between 25- and 250-m depth in the upper ocean.

[20] In this paper we focus on data returned by AOFB-3, deployed at NPEO in 2004, and AOFB-4, deployed at NPE0 in 2005, hereafter referred to as buoy 3 and buoy 4, respectively. These buoys were chosen for analysis because they obtained high-quality turbulent shear stress records.

[21] Buoy 3 was installed near the center of a largely circular floe with a diameter of 300–600 m. It was collocated with a PMEL met station and a CRREL IMB (ID Code NP7100). A JCAD buoy was deployed from the 2003 NPEO camp, but it was installed several hundred km away, on the opposite side of the Lomonosov Ridge. Buoy 3 began transmitting data on 27 April 2004 at a position about 72 km from the geographic North Pole along longitude 123°E. Surface currents transported buoy 3 across the Eurasian Basin, out of the Arctic Ocean along the eastern side of Fram Strait, and into the East Greenland Current (Figure 2). The buoy survived for more than 80 days in the persistent tongue of ice off the east coast of Greenland. On the basis of the variance of the fluctuating quantities, we estimate the buoy encountered open water on 20 April 2005. The last data transmission occurred on 08 May 2005, at which point it was 2500 km from its starting position and had drifted a total distance of 3902 km along its trajectory.

[22] There are occasional gaps in the buoy 3 records presumably due to rhiming of the antenna cover radome. For a 21-day-long period between 10 July 2004 and 31 July 2004 (yeardays 192–213), buoy 3 reported anomalously large stress estimates. Video images taken from the PMEL meteorological installation document the buoy breaking through the bottom of a melt pond that had formed around it during this period. The bobbing about of the buoy in the weak ice apparently contaminated the flux estimates; so data from this period are discarded. After 31 July 2004, ice solidified around the buoy, and the stress estimates were fine for the remainder of the buoy lifetime.

[23] Buoy 4 was deployed on 27 April 2005 (just days before its predecessor stopped transmitting offshore of Greenland) at a position about 61 km from the Pole along longitude 145$^o$ E. It was collocated with a PMEL met station, a CRREL IMB (ID Code 09114), and a JCAD (ID Code 9). The trajectory of buoy 4 was very similar to that of buoy 3 (Figure 2). We estimate that the buoy encountered open water on 07 January 2006; and the final

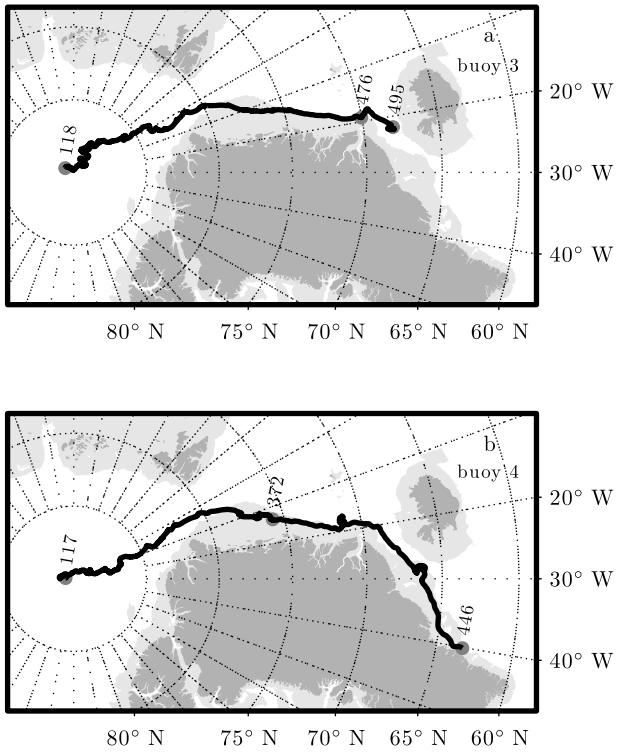


**Figure 2.** Maps of (a) buoy 3 and (b) buoy 4 drift trajectories. Shading indicates the coastline and the 500-m isobath. The gray dots along the drift tracks mark the yearday of deployment, open water encounter, and final transmission, respectively. Analysis is limited to data collected before the buoys enter open water.

data transmission occurred on 22 March 2006, at which point it was 3048 km from its starting position over the Greenland Sea continental shelf, having covered a distance of 5088 km along its trajectory.

[24] In contrast to the buoy 3 deployment site, buoy 4 was installed near the center of a relatively small and elongated floe, with prominent (~1-m surface expression) pressure ridges delineating the long edges. The width of the floe, i.e., the distance between the ridges, was ~50 m. Buoy 4 and JCAD-9 were installed at opposite ends of the floe, along its long axis (Figure 3). GPS positions from the two sites and headings recorded onboard the buoy from the ADCP compass, determine the orientation of the current meter instrument coordinate systems with respect to the heading of the two ridges. The traveltime current meter coordinate system was aligned such that flows in the directions 90–180° (quadrant II) and 270–360° (quadrant IV) were more exposed to the upstream disturbance of the pressure ridge keels (i.e., shorter distance from the buoy to the ridges) than flows in the directions 0–90° (quadrant I) and 180–270° (quadrant III) (Figure 3).

[25] Although our focus here is on a statistical assessment of the ice underside roughness length, we briefly present here an overview of the buoy 3 and buoy 4 data sets from a time series perspective (Figures 4 and 5) before moving on to heavily averaged results.

[26] As expected, both buoys responded primarily to ice motions forced by the passage of atmospheric pressure systems with timescales of several days. This is evident in the covarying time series of GPS-derived ice speed $V_0$ and the friction speed measured by the flux package $u_{*m}$ (Figures 4b and 5b). Ice and friction speeds were smaller over the Arctic Eurasian Basin than in Fram Strait or the Greenland Sea, where climatological wind speeds are larger. The correlation between $V_0$ and $u_{*m}$ lends confidence to the stress estimates. Ice drift speeds during strong forcing events of the buoy 3 drift (the average of the largest 10% of $V_0$ was 0.37 m s$^{-1}$) were generally larger than those observed during the buoy 4 drift (average of largest 10% of $V_0$ was 0.30 m s$^{-1}$). In contrast, friction speeds during the strong forcing events were larger in the buoy 4 record then the buoy 3 record (averages of the largest 10% of $u_{*m}$ were 0.010 m s$^{-1}$ and 0.014 m s$^{-1}$, for buoys 3 and 4, respectively), providing an immediate indication that the buoy 4 floe was locally rougher than the buoy 3 floe.

[27] Records of ADCP shear from both buoys (Figures 4c and 5c) contained near-surface shear in the ocean boundary layer that results from storm-forced surface stress and rotational shear in the outer part of the boundary layer. Near-surface shear is evident most clearly during the larger storms that occurred in the later stages of both records when the buoys were in Fram Strait or the Greenland Sea. Another prominent feature of the ADCP observations is large shear at the base of the well-mixed layer. This allows the ADCP records to be used to trace the evolution of the mixed layer depth. For example, the formation of a thin surface mixed layer during the onset of ice melt is clearly visible in both records starting at about yearday 200 as is the deepening of this layer by surface forcing after its initial formation continuing through day 300. For buoy 4, there is good agreement between the depth of elevated ADCP shear

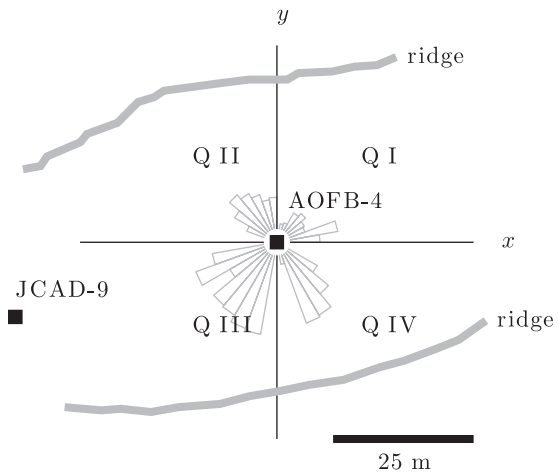


**Figure 3.** Sketch of the floe on which AOFB-4 was deployed. The locations of AOFB-4 (buoy 4) and JCAD-9 are indicated with squares. The approximate positions of the two large pressure ridges discussed in the text with respect to the traveltime current meter instrument coordinate system ($x - y$) are indicated with gray lines. The line between the positions of AOFB-9 and JCAD-9 established the long dimension of the floe. Also shown is a histogram of ensemble flow directions used for the analysis. Gaps along the directions of the instrument coordinate axes result from the path switching problem discussed in the text.

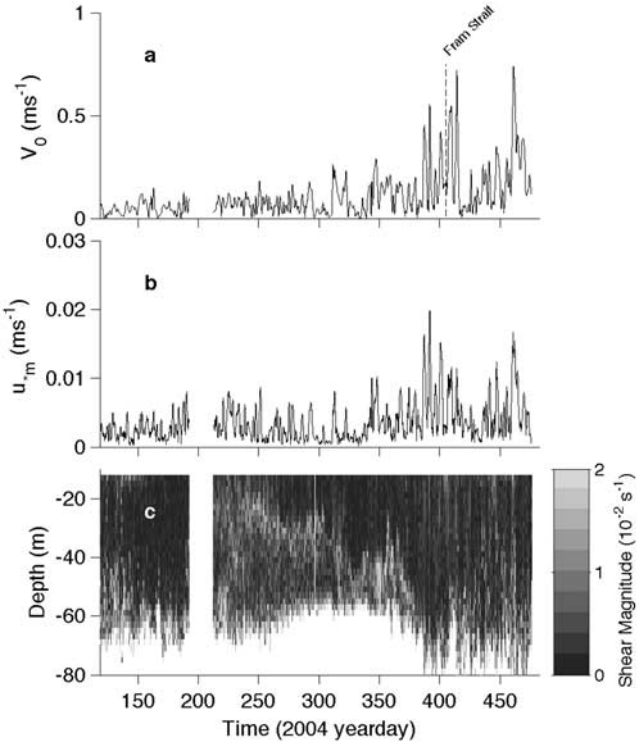


**Figure 4.** Time series summary of buoy 3 data set: (a) ice speed $V_0$, (b) measured friction speed $u_{*m}$, and (c) ADCP shear magnitude. The $V_0$ and $u_{*m}$ records are smoothed with a 12-h boxcar filter for plotting. The dashed vertical line in Figure 4a indicates the time that the buoy entered Fram Strait.

and the mixed layer depth estimated from buoy 4 and JCAD-9 data set (Figure 5d, see section 5.1 for description of the mixed layer depth estimation). These results also highlight the sensitivity of outer boundary layer currents to the vertical structure of density, as described in more detail in section 5.

## 4. Roughness Length: Stress-Based Estimates

[28] Using (4), the law of the wall provides estimates of surface roughness as long as the shear stress and velocity are measured within the log and constant stress layers. Roughness length $z_0$ represents an inherent property of the interface, so if the law of the wall is satisfied, estimates of $\nu_m$ should be independent of surface stress and/or ice speed. As discussed in section 2, however, the depth of the AOFB flux package is purposely set relatively deep in the IOBL so that the flux estimates have a large upstream fetch. We expect departures from the law of the wall to occur during periods of weak surface forcing when the scaled measurement height $\eta$ is relatively large and the measurement height is beyond the outer edge of the log layer. In this section, we first show that $\nu_m$ varies in the manner just described and that the law of the wall does not apply to the majority of the samples in the two buoy data sets. In an effort to quantify and remedy the errors encountered when applying (4) to our data sets, we then develop an extension to the law of the wall that allows application deeper in the boundary layer. Finally, we present the results obtained by applying the extended version to the buoy data sets by quadrant of flow direction at the traveltime current meter, as discussed in section 2.

### 4.1. Variability of the Local Drag Coefficient With Ice Speed

[29] The approach to demonstrating that $\nu_m$ is dependent on the surface forcing, and therefore on $\eta$, is to average individual, 4-h estimates $U_m$, $u_{*m}$ and their ratio $\nu_m$ over bins of $V_0$ for each buoy (Figure 6). Ice speed, with the near-inertial component removed by band stop filtering, is used as a surrogate for surface forcing here (rather than measured shear stress) because the self-correlation of the noisy stress estimates (see section 3) creates large, undesired variability in binned $\nu_m$ estimates. The inertial component of the ice velocity is removed because, for inertial motions, ice and IOBL fluid velocities are approximately equal and make little contribution to production of turbulence.

[30] The relationship between $U_m$ and $V_0$ (Figures 6a and 6b) provides a nice description of how boundary layer depth varies in comparison to the measurement depth $z_m$. For both of the data sets, $U_m$ is approximately equal to $V_0$ (the velocities are equal and opposite), for values of $V_0$ less

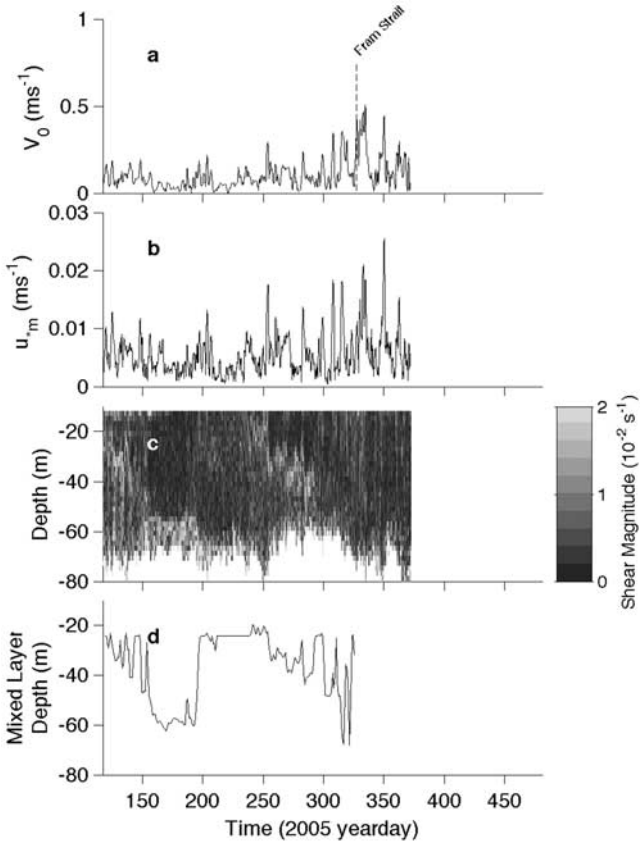


**Figure 5.** Time series summary of buoy 4 data set: (a) ice speed $V_0$, (b) measured friction speed $u_{*m}$, (c) ADCP shear magnitude, and (d) estimate of mixed layer depth from the buoy 4 and JCAD-9 data set. The $V_0$ and $u_{*m}$ records are smoothed with a 12-h boxcar filter for plotting. The dashed vertical line in Figure 5a indicates the time that the buoy entered Fram Strait.

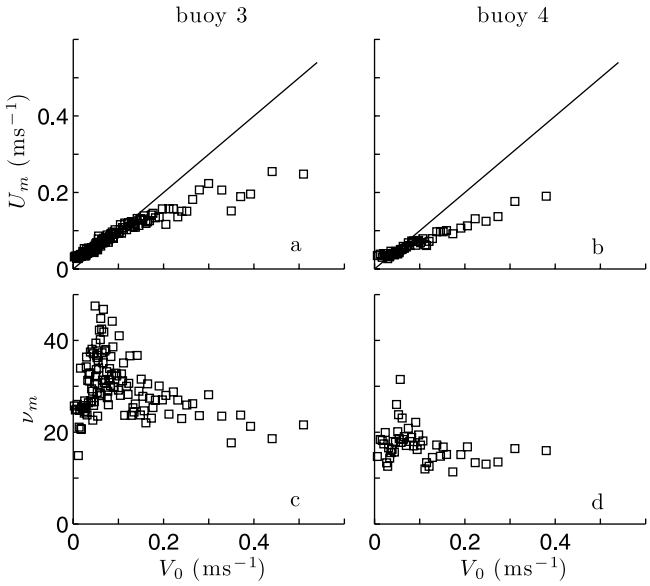


**Figure 6.** Speed measured by the traveltime current meter $U_m$ bin averaged as a function of ice speed $V_0$ for (a) buoy 3 and (b) buoy 4. Dimensionless speed $\nu_m$ bin averaged as a function of $V_0$ for (c) buoy 3 and (d) buoy 4.

than 0.1 m s$^{-1}$, This indicates, as expected, that for weak surface forcing, $z_m$ is essentially outside of the boundary layer. Stated alternatively, the boundary layer thickness is comparable to $z_m$ (5 m) for ice speeds close to 0.1 m s$^{-1}$. For $V_0$ greater than 0.1 m s$^{-1}$, $U_m$ is smaller than $V_0$, and the difference between the two quantities increases with increasing $V_0$. This is a direct consequence of $\eta$ decreasing with increasing $V_0$ as the boundary layer grows in response to stronger surface forcing: the thicker the boundary layer, the relatively closer the measurement depth is to the highly sheared and flow-retarded log layer.

[31] The variability of $\nu_m$ as a function of $V_0$ (Figures 6c and 6d) is consistent with our expectations. The ratio initially increases with increasing $V_0$, reaches a maximum, and then decreases with increasing $V_0$. The region of increasing $\nu_m$ results from the noise floor in the $u_{*m}$ mentioned in section 2. The more physically significant behavior occurs for ice speeds greater than 0.1 m s$^{-1}$. Above this threshold, $\nu_m$ asymptotically approaches a constant value with increasing speed. The behavior is consistent with $\eta$ decreasing to be within the log layer, where $\nu_m$ is predicted to be constant by (4), as the boundary layer deepens in response to strong surface forcing. Presented this way, the data confirm that the measurement depth was often too deep in the IOBL for the law of the wall to hold.

### 4.2. Extension of the Law of the Wall

[32] The local estimates of drag presented in the previous section are smaller for weak forcing ($\nu_m$ increases as $V_0$ decreases) than for strong forcing because two factors contribute to a failure of the law of the wall when the scaled measurement height $\eta$ is large. First, the measured shear stress is considerably attenuated from the interface value (i.e., the measurement depth is beyond the approximately constant stress layer). When $u_{*m} < u_{*0}$, roughness length estimates based on (4) are biased low. Second, the Ekman boundary layer length scale has a significant dynamic effect on the velocity profile. As we will show below, realistic outer boundary layer currents have greater shear than predicted by the law of the wall; so roughness estimates based on (4) are also biased low when the effect of the Ekman scale on the velocity profile is significant.

[33] Because the law of the wall does not apply directly to most of the flux package data collected by buoy 3 and buoy 4, we formulate a simple extension of the law of the wall with the goal of producing a model of the boundary layer flow that can be used above the region of approximate constant stress and where the mixing length is affected by the Ekman length scale in addition to distance from the interface. The extension to (4) is a mixing length model in which vertical velocity shear is proportional to the local friction velocity $u_*$ multiplied by a turbulent length scale $\lambda$. An assumption about the stress distribution across the boundary layer is introduced to relax the constant stress assumption. A parameterization of the turbulent length scale in the outer part of the boundary layer is introduced to relax the assumption that distance from the interface is the only significant length scale. The approach is similar to that of *McPhee* [2002]; the primary difference is that McPhee used an observational determination of the turbulent mixing length, while here it is parameterized. The model is simple, it does not attempt to account for buoyancy effects resulting from either surface buoyancy fluxes or stratification at the base of the mixed layer. Yet, the extension does provide a method for estimating the surface roughness length for data taken beyond the strictly logarithmic and constant stress layers, which is useful for these data sets. The technique allows more data points to be used for estimating roughness length, which is useful for this study, and it quantifies the magnitude of the error used when roughness is calculated using the law of the wall in its original form, which may be useful for other studies as well.

[34] On dimensional grounds, the vertical structure of the boundary layer currents is hypothesized to depend only on the turbulent mixing length and the local friction velocity through the nondimensional combination $u_*/\lambda$

$$\frac{du}{dz} = u_* \lambda^{-1} \tag{7}$$

Here $u_*$ and $\lambda$ are the local, depth-dependent variables which must be prescribed by the model. If the turbulent length scale is controlled exclusively by distance from the interface, i.e., $\lambda = \kappa z$, and $u_*$ is approximately constant and equal to $u_{*0}$, then a vertical integration of (7) results in the law of the wall (2).

[35] In the model,we assume that friction speed has a linear distribution across the boundary layer

$$u_*(z) = u_{*0}\left(1 - \frac{z}{h}\right), \tag{8}$$

varying from $u_{*0}$ at the interface to zero at the outer edge of the boundary layer at depth $h$. The constant stress layer therefore occupies a small fraction of the total boundary layer. Rossby similarity provides the scale for boundary

layer depth $h_E$ and numerous studies [e.g., *Coleman*, 1999] have tried to provide the similarity constant $C$ that relates scale depth to physical depth $h_E$

$$h_E = C\frac{u_{*0}}{f}. \tag{9}$$

Here, we neglect any possible stratification effects on $h_E$ and take $C = 0.5$ [*Coleman*, 1999].

[36] Following *McPhee* [1994], the basic idea of the length scale parameterization is that in the outer part of the boundary layer, boundary layer depth is a dynamically significant length scale that limits eddy size and it is the smaller of the length scales imposed by distance from the interface or rotation that sets the turbulent mixing length. This physical insight is implemented with a simple prescription for $\lambda$

$$\lambda^{-1} = \left(\frac{1}{\kappa z} + \frac{1}{\Lambda_* h_E}\right) \tag{10}$$

Here $\Lambda_*$ is a similarity constant with value 0.028 [*McPhee*, 1994] that relates $h_E$ to a maximum turbulent length scale. Relatively close to the interface, $\lambda$ behaves like $\kappa z$ and the law of the wall holds. Relatively deep in the boundary layer, $\lambda$ asymptotes to the depth-independent value $\Lambda_* h$ and the law of the wall is modified. Essentially, the parameterization imposes a maximum turbulent length scale that is set by the Ekman depth and which limits eddy size in the outer part of the boundary layer.

[37] Combining (7), (8), (9), and (10) yields an expression for boundary layer shear

$$\frac{dU}{dz} = u_{*0}\left(1 - \frac{Cz}{h_E}\right)\left(\frac{1}{\kappa z} + \frac{1}{\Lambda_* h_E}\right). \tag{11}$$

Integrating (11), while assuming $z \gg z_0$, yields the extended law of the wall, a log-quadratic velocity profile

$$\frac{U}{u_{*0}} = \frac{1}{\kappa}\ln\frac{z}{z_0} + \alpha\eta - \beta\eta^2. \tag{12}$$

where

$$\alpha = \frac{1}{\Lambda_*} - \frac{C}{\kappa}, \quad \beta = \frac{C}{2\Lambda_*}.$$

As desired, the linear and quadratic correction terms to the logarithmic profile are functions of the scaled measurement height. Because $\Lambda_*$ is a small number, the linear correction term is dominated by the limiting effect of the Ekman scale on the turbulence scale. Within the boundary layer, the quadratic correction term is smaller than the linear term. At the outer edge of the boundary layer as specified by (9), the linear correction is approximately eight times greater than the quadratic correction. The effect of the corrections, which are comparable in magnitude to $U_m/U_{*0}$ beyond the near-interface region, is to increase outer boundary layer shear above the levels predicted by the law of the wall.

[38] The extended law of the wall cannot be applied directly to measured current and friction speed to estimate $z_0$ because (12) is formulated with $u_{*0}$ as the velocity scale. The assumed shear stress distribution (8), though, provides the required relationship between stress measured at depth $z_m$ and stress at the interface

$$u_{*0} = u_{*m} + \frac{fz_m}{C}. \tag{13}$$

So, from an observational perspective we use a two step procedure to estimate $z_0$ from measured $\nu_m$. First adjust the measured stress to the interface value with (13), then use (12) to account for additional shear in the velocity profile.

### 4.3. Results

[39] We apply the extended law of the wall (12) to velocity data that are bin-averaged as a function of the normalized depth $\eta$ and quadrant of flow direction measured by the traveltime current meter (Figure 7). The $\eta$ dependence of $\ln(z_m/z_0)$ estimates made using (12) is investigated to determine if the application of $\alpha$ and $\beta$ correction terms to measured local drag can correct the stress dependence of roughness estimates seen in Figure 6. Variability as a function of flow direction provides an indication of the effects of interface morphology heterogeneity and of how spatially representative the roughness estimates are.

[40] We start by recasting the dimensionless speed estimated from the buoy 3 and buoy 4 data sets (previously plotted as a function of ice speed in Figure 6) as a function of $\eta$ (Figures 7a and 7b). For both data sets, $\eta$ is distributed between 0.05 and 0.25 which translates to the measurement height being equal to 10% of the boundary layer height for the largest stresses and to 50% of the boundary layer height for the smallest stresses used in the averaging (the minimum $u_{*m}$ condition of 0.0025 m s$^{-1}$ is applied here). The extended model provides the framework for interpreting the observed $\eta$ dependence of $\nu_m$.

[41] Also immediately visible in Figures 7a and 7b is a substantial variability of $\nu_m$ with quadrant of flow angle. For buoy 3, quadrants II, III, and IV have similar drag distributions, with $\nu_m$ increasing from about 15 to 25 over the observed range of $\eta$. Quadrant I has values that are about 20% larger than the other directions; presumably this is due to rougher upstream under-ice morphology in this direction, but we have no observations to confirm this. For buoy 4, $\nu_m$ estimates in quadrants I and III are similar to or slightly less than quadrants II, III, and IV of buoy 3. Values of $\nu_m$ in quadrants II and IV are about 20% smaller than the others indicating that flow felt a rougher interface in those directions, which correspond to the flows obstructed by ice ridge keels (Figure 3). The standard errors of the binned $\nu_m$ estimates are about 10%, so these differences as a function of flow disturbance are statistically significant.

[42] For the assumed linear friction speed vertical profile, the adjustment from measured friction speed to interface friction speed in the ratio of current to friction speed (Figures 7c and 7d) is a simple additive correction with numerical value $1.6 \times 10^{-3}$ m s$^{-1}$. For the friction speeds used in the averaging, the adjustment is significant, 11% to 63% of the measured $u_*$ value. With the velocity scale adjusted, the $\alpha$ and $\beta$ corrections can then be applied to $U_m/u_{*0}$. The linear correction (Figures 7c and 7d) increases from a numerical value of 2 to a value of 10 over the

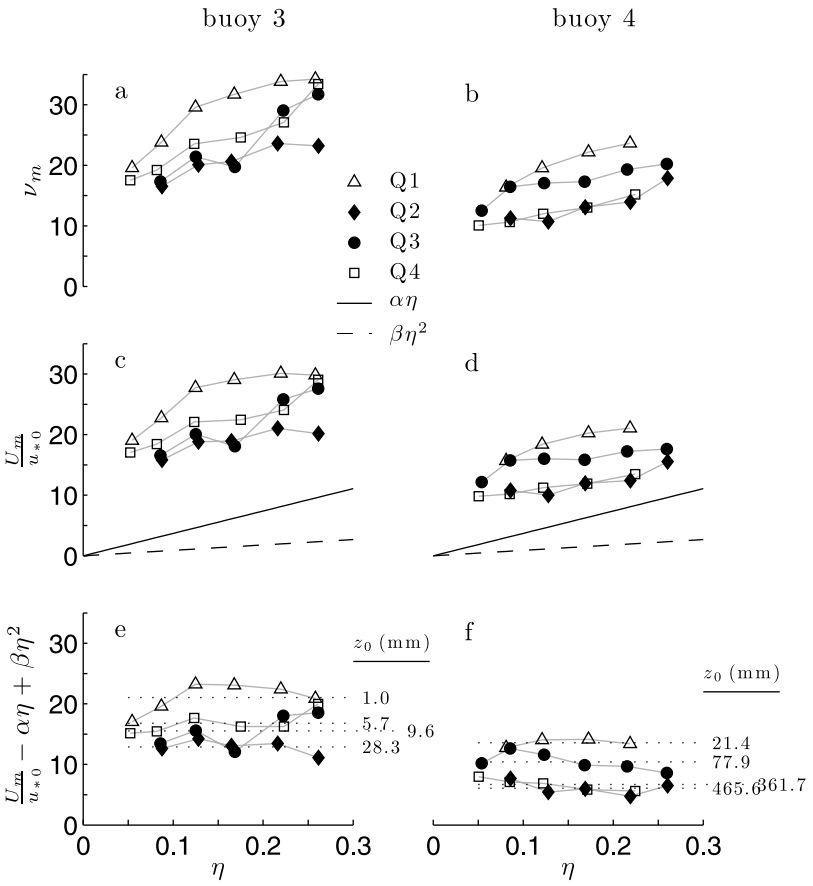


**Figure 7.** Roughness length estimates based on the extended law of the wall. Data points in the plots are bin averages as a function of scaled measurement depth $\eta$ and quadrant of flow direction, Q I, Q II, Q III, and Q IV. Dimensionless speed $\nu_m$ for (a) buoy 3 and (b) buoy 4. Ratio $U_m/u_{*0}$ for (c) buoy 3 and (d) buoy 4. Quantity $U_m/u_{*0} - \alpha\eta + \beta\eta^2$, which is the extended law of the wall estimate of $1/\kappa \ln(z_m/z_0)$, for (e) buoy 3 and (f) buoy 4. The $\alpha$ and $\beta$ correction terms are shown in Figures 7c and 7d. Average $z_0$ estimates by quadrant are indicated in Figures 7e and 7f.

observed $\eta$ range. This is an important term, representing a 10% to 40% correction, with the physical interpretation that the Ekman layer scale is dynamically important at the measurement height. The quadratic $\beta$ correction is small, and not important for the range of friction speeds considered.

[43] Finally, we consider the quantity $U_m/u_{*0} - \alpha\eta + \beta\eta^2$ (Figures 7e and 7f), which is the estimate of $\ln(z_m/z_0)$ in the extended model (12). Compared to $\nu_m$ (Figures 7a and 7b), the dependence of the corrected estimates on $\eta$ has been greatly reduced. This result lends credence to the extended model, suggesting that outer layer effects have been reasonably well described. Resulting $z_0$ estimates, made by averaging over $\eta$, vary considerably as a function of flow direction. For buoy 3, $z_0$ is estimated as 28 mm, 9.6 mm, and 5.7 mm for quadrants II, III, and IV, respectively. Buoy 3 quadrant I flows apparently experienced smoother upstream conditions, as $z_0$ for this quadrant is estimated as 1.0 mm. For buoy 4, $z_0$ is estimated as 21 mm and 78 mm for quadrants I and III. The roughness length for flows obstructed by ice ridge keels is about an order of magnitude larger than unobstructed directions: 466 mm and 362 mm for quadrants II and IV. The observed variation with flow direction for buoy 4 indicates that the estimates are sensitive to local morphological variation even though the measurement depth was set relatively deep in the boundary layer. This is not too surprising because the nearby ice ridge keels are expected to have had a large effect on the flow, and the depth of the keels must have been comparable to the depth of the measurements. Including data from all quadrants, the average roughness lengths for the buoy 3 and buoy 4 data sets are 5 mm and 140 mm, respectively.

[44] These point-measurement-based roughness estimates are troublesome from the scaling-up perspective. On large scales, pressure ridge systems in pack ice tend to have random orientations, so that at the scale of multiple floes, we do not expect roughness to be directional. This is the scale that is relevant for all but the most detailed of modeling efforts. There are efforts to model the details of boundary layer flows over ice ridge keels [e.g., *Skyllingstad et al.*, 2003] and we are pursuing the topic observationally with the AOFB data sets.

## 5. Roughness Length: Outer Layer Velocity Modeling

[45] The directionality of the extended law of the wall $z_0$ estimates suggests that spatially representative roughness

estimates require methods with larger fetches than is feasible with stress-based methods. A novel technique for estimating undersurface roughness, developed from analysis of ocean drag on multiyear sea ice in the western Weddell Sea [*McPhee*, 2008] provides an alternative method for estimating representative roughness. It is based on modeling mean velocity characteristics in the outer part of the IOBL over a range of prospective undersurface roughness values, choosing the one that best matches observations in a mean sense. The underlying premise is that at levels deeper in the IOBL, local differences in under-ice roughness become less important in determining boundary layer shear, thus deeper measurements are more representative of the larger-scale surroundings. The method requires both good velocity measurements in the outer boundary layer (where angular shear is pronounced) and a reasonably accurate estimate of temperature and salinity gradients in the upper ocean. Because the 2004 JCAD deployment was not collocated with buoy 3 (it was installed several hundred km away), the technique is only applied to the 2005 buoy 4 deployment data.

### 5.1. Outer Boundary Layer Velocity Profiles

[46] Despite large sample-to-sample variation, nearly every 4-h ADCP profile average examined from the buoy 4 deployment exhibited clockwise turning with increasing depth indicating Ekman (Coriolis) turning. We nondimensionalized individual 4-h average velocity profiles by the velocity at a reference level chosen typically below the bulk of the angular shear. In Figure 8 the nondimensional hodographs, classified according to three speed ranges for the reference velocity at 32 m are shown. The angular shear at middepth in the boundary layer (e.g., 16 m) increases noticeably with increasing current speed, as would be expected if the boundary layer scaling responds to dynamic scaling, for example, proportional to $u_{*0}/f$, rather than say distance from the interface.

[47] The combination of buoy 4 flux package sensors and the nearby JAMSTEC JCAD-9 buoy provided discrete temperature and conductivity measurements at seven nominal depths ranging from 7.6 to 285 m, where the actual depths varied upward depending on the drag exerted on the suspended cable. Modeling described in the next subsection requires continuous density profiles in the upper ocean, with a reasonably accurate estimate of the depth of the well mixed layer, $d_{ml}$. For most of the data record, $d_{ml}$ fell between the 2nd and 3rd clusters (i.e., between 24 and 48 m); hence there were usually five instrument pairs in and below the pycnocline. Since density is controlled mainly by salinity at low temperatures in the polar oceans, we developed a method for estimating salinity profiles and $d_{ml}$ by performing a four-parameter, nonlinear least squares regression of the depth (d) and salinity (S) value pairs beginning with the first cluster where salinity exceeded the surface value by 0.03 psu:

$$S(d) = S_0 + a(d - d_1) + b\left[e^{-\alpha(d-d_1)} - 1\right] \qquad (14)$$

where $d_1$ is the depth of the first cluster within the pycnocline. Mixed layer depth is estimated by extending this function upward until the fitted salinity matches the observed salinity as measured at the deepest instrument level still considered in the well mixed layer (Figure 9). When more than two *T*/*C* instrument clusters were in the well mixed layer, the fit is underdetermined, and for those instances we estimated the mixed layer depth from shear observed in the ADCP profile, adding a point with this depth and mixed layer salinity to the nonlinear regression. Temperature has little impact on density at low upper ocean temperatures encountered during the drift; hence profiles were estimated by linear interpolation between instrument levels. Mixed layer depth estimates are shown in Figure 5d.

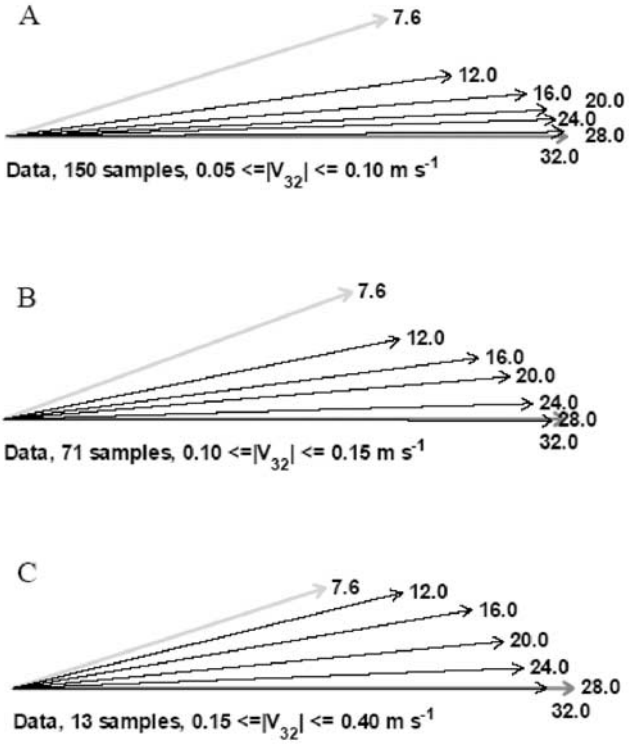


**Figure 8.** Average nondimensional hodographs of horizontal velocity relative to the 32-m level for three different speed ranges: (a) 0.05–0.10 m $s^{-1}$, (b) 0.10–0.15 m $s^{-1}$, and (c) 0.15–0.40 m $s^{-1}$, where the maximum observed speed was about 0.4 m $s^{-1}$. Numbers indicate the depth in meters. The topmost vector, labeled 7.6, is from the traveltime current meter on buoy 4, while the remainder are from the buoy 4 ADCP. Averages were formed by classifying each 4-h ADCP profile according to speed at 32 m, dividing complex vectors at the sample levels by the 32-m vector, and averaging the number of samples in each speed category as listed.

### 5.2. SLTC Model

[48] The nondimensional hodographs (Figure 8) suggest that the method developed by *McPhee* [2008] for estimating $z_0$ representative of a heterogeneous, multiyear ice floe in the western Weddell Sea might be applicable to the buoy 4 data set. The steady local turbulence closure (SLTC) model [*McPhee*, 1999] assumes that turbulence adjusts instantaneously to ice/ocean interface flux conditions and to the prescribed density structure in the upper ocean. It utilizes an iterative scheme that begins by assuming no stratification in the upper ocean, solving the IOBL momentum equation

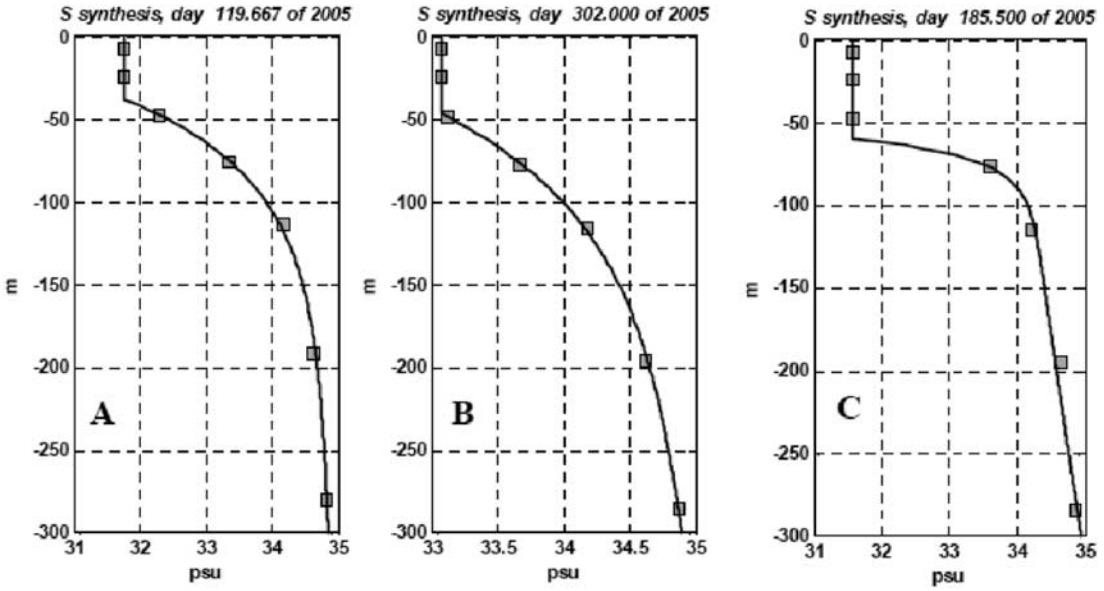


**Figure 9.** Salinity profiles synthesized from measurements at discrete depths (square symbols) by nonlinear least squares regression, from (a) early in the drift, (b) late in the drift, and (c) for a time when the mixed layer was deeper than 48 m. For the last, an independent estimate of $d_{ml}$ based on ADCP shear provided an extra point in the regression analysis.

(without local inertia) following similarity scaling that takes into account both interfacial stress and buoyancy flux [*McPhee*, 1981]. Given a first estimate of IOBL shear and turbulence scales (hence eddy diffusivity), profiles of heat and salt flux are calculated from the prescribed temperature and salinity structure. In the next iteration, the calculated IOBL buoyancy flux is included in a new eddy viscosity calculation, and the momentum equations are solved again. This is repeated until the difference between successive iterations is small enough to meet a convergence criterion. By including buoyancy flux throughout the IOBL, the model can account, for example, for a relatively shallow well mixed layer where stress near the top of the pycnocline is an important element of the overall momentum structure, affecting both the drag and the amount of angular shear in the IOBL. The advantage of the technique over time-dependent numerical models with similar or analogous closure is that it can be applied to particular instantiation of any data set that includes suitable velocity (or stress), temperature, and salinity measurements.

[49] In the present application, local stress measured near the interface may not be representative of the overall stress on the floe, so is not used to force the model. Instead, an outer iteration loop matches velocity measured at a particular level relative to the drifting ice. We chose a level that is shallow enough to be within the outer (Ekman) IOBL (i.e, where there is angular shear) yet deep enough to be relatively uninfluenced by the under-ice morphology in the immediate vicinity of the measurement site: in our case, the observed hodographs (Figure 8) suggest that 20 m below the interface is an acceptable choice.

[50] In the first step of the outer iteration loop, vector (complex) interface friction velocity, $\mathbf{u}_{*\mathbf{0}}$, is estimated using the Rossby similarity drag law (5). Interface buoyancy flux is then estimated by an interface submodel [e.g., *Notz et al.*, 2003] from $\mathbf{u}_{*\mathbf{0}}$, and mixed layer (far-field) temperature and salinity. With the interface conditions and prescribed T/S profiles (section 5.2), the model is solved for velocity at the reference level. In general, this will not match the observed reference velocity after the first iteration, so $\mathbf{u}_{*\mathbf{0}}$ is adjusted by the complex ratio of observed to modeled reference velocity, and the procedure repeated until the difference in $\mathbf{u}_{*\mathbf{0}}$ is negligible.

[51] An example of one model realization is illustrated in Figure 10, for a 4-h average of data, centered at time 255.667 (12 September 2005, 1600 UT). The model hodograph (dotted curve) has been translated to match the velocity structure seen by an observer on the drifting ice, where shear between the ice and uppermost grid point in the model is in the direction of surface stress and calculated with $z_0 = 0.09$ m. Given the approximations inherent in the model (steady state; density structure synthesized from discrete levels; no geostrophic shear; etc.), the difference between modeled and observed velocities (arrows) at discrete levels is not surprising. Averaged over many realizations, we expect these to even out.

### 5.3. Results

[52] Following the approach of *McPhee* [2008], the model was run for all 4-h samples for which the magnitude of the reference velocity at 20 m exceeded 0.1 m $s^{-1}$ and for several different values of surface roughness. By evaluating velocity at sample levels as illustrated in Figure 10 for each model realization, nondimensional model profiles were evaluated and then averaged for comparison with the averaged observations.

[53] We used angular shear between the 11 and 31 m depths as the criterion for choosing the best match between model and data. Although somewhat arbitrary, these levels

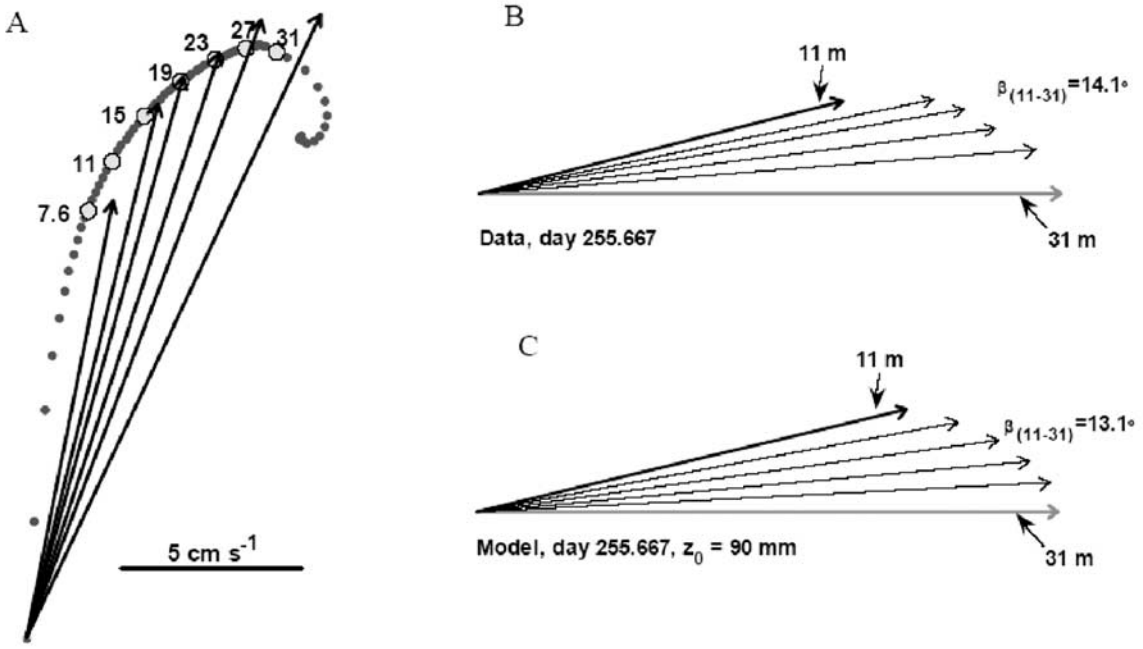


**Figure 10.** (a) Model hodograph (dotted curve) derived from a 4-h average of buoy 4 data centered at time 255.667, for an observer drifting with the ice. Up is approximately north. Numbers indicate depth; the model assumes that ice draft is 2.5 m. Arrows are the observed currents at the same depths. (b) Nondimensional hodograph from the ADCP profiles sampled at 4-m intervals from 11 to 31 m. Angular shear in the ADCP profile is indicated by $\beta$. (c) Same as Figure 10b, except modeled velocities are nondimensionalized by the modeled current at 31-m depth.

nearly always spanned the distance between the first acceptable ADCP measurement bin and the depth of the dynamic boundary layer. The flux package measures currents at 7.6 m; however, as shown before, this level was apparently often significantly affected by the local topography, and our basic premise is that conditions lower in the boundary layer will more accurately reflect the area-averaged conditions. Given the large variation in $z_0$ inferred from local stress and velocity measurements when the flow approached from different quadrants as identified in section 4.3, we classified the model realizations according to the flow direction at 7.6 m and searched for $z_0$ values that best matched the angular shear (Figure 11). For quadrants II through IV, model averages with $z_0$ values ranging from 0.04 to 0.13 m were found to match observed angular shears. For quadrant I, $\beta$ was better matched with $z_0$ an order of magnitude smaller. However, in this quadrant there was significantly more distortion of the mean data hodograph at shallower depths, in particular, more angular shear between 7.6 and 11 m, indicating possible formation of an interior Ekman layer embedded within the overall IOBL structure. A similar phenomenon was encountered under an expanse of hydraulically smooth ice embedded in the multiyear ice pack during the Arctic Internal Wave Experiment [see *McPhee*, 1990, Figure 6.9].

[54] Combining all of the 4-h averages except those in quadrant I, the overall best match for modeled and observed angular shear occurred for $z_0$ = 0.09 m (Figure 12). Turbulent stress in the model is calculated from the product of eddy viscosity and velocity gradient. It and the mean velocity relative to the surface were calculated at model depth 5.1 m (assuming 2.5 m ice draft), with mean values listed in Figure 12. These differ from the mean observed values by less than 10%, when all of the samples except those from quadrant I (34 samples) are averaged. As discussed in section 1, the ratio of current speed to friction speed is a useful indicator of surface roughness. Again, the mean modeled and observed values are reasonably similar. Despite large differences in this ratio depending on current direction (average values for quadrants I–IV are 22.8, 10.4, 16.3, 11.0, respectively), it appears that for overall averages, the choice of 5 m below the ice for the flux instrument level was not unreasonable.

[55] The model may be used to estimate the attenuation of Reynolds stress from the interface to the measurement level. The mean value of $u_{*m}/u_{*0}$, where $u_{*m}$ is evaluated at the flux instrument level, is 1.19, i.e., approximately a 40% reduction in stress from the interface to a level 5.1 m lower, which is larger than the prediction of the simple linear variation of $u_*$ used in section 4.2.

[56] The model results (189 4-h realizations) were also used to evaluate the parameters (with standard deviations) in the Rossby similarity inverse drag law (5): $A = 2.39 \pm 0.12$; $B = 2.27 \pm 0.16$. Mean values for magnitude and turning angle of the model calculated $\mathbf{V_0}/\mathbf{u_{*0}}$ are 12.4 and 27.3° respectively. The Rossby similarity factors are similar to values obtained from an analytic two-layer similarity solution assuming neutral stratification: A = 2.2; B = 2.3 [*McPhee*, 1990]; however, $\mathbf{V_0}/\mathbf{u_{*0}}$ calculated from the SLTC model (which includes the effect of stratification in the upper pycnocline) differs from the Rossby similarity function (5) by (i) having slightly higher nondimensional surface

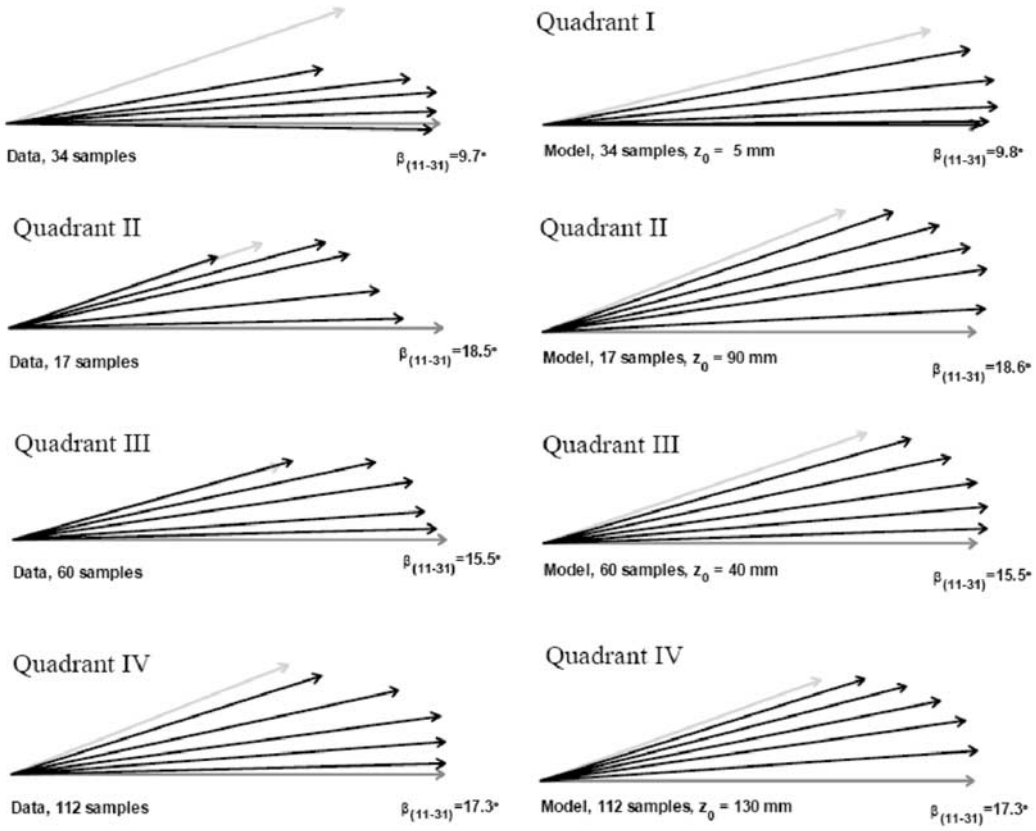


**Figure 11.** Nondimensional hodographs, (left) observed and (right) modeled for the four quadrants identified in section 3. The number of 4-h average realizations for which the reference velocity (at 20 m) exceeded 0.1 m $s^{-1}$ in magnitude is listed, along with the values of $z_0$ that provided the closest match for angular shear between 11- and 31-m depth.

velocity (lower geostrophic drag), and (ii) showing an increase in the turning angle magnitude with speed. Both effects are consistent with a relatively shallow pycnocline depth compared with the dynamic IOBL depth for higher current speeds.

## 6. Discussion and Conclusions

[57] The most common method for estimating surface roughness in geophysical boundary layers is to apply the law of the wall to near-boundary observations. In an environment with heterogeneous boundary morphology like the IOBL the desire to use measurements as deep in the boundary layer as possible in order to have a large upstream fetch conflicts with the requirement that the measurement be close to the boundary to satisfy the law of the wall. The extension to the law of the wall presented here acknowledges that as distance from the boundary increases: (i) stress magnitude decreases; and (ii) the governing turbulence scale no longer depends solely on $z$. Possible refinements could include implementing a less simplistic specification of the vertical stress profile, perhaps an exponential profile over the Ekman scale. The SLTC model results predict, for example, that there is more stress attenuation than used in the extended law of the wall model. Local buoyancy effects could be included, if necessary, through the use of the Monin-Obukov similarity theory. For the data sets considered here, the measurement depth of about 5 m appears to be a reasonable compromise between applying the extended law of the wall and having a large upstream footprint: the corrections applied to the largest stress events are not too large. Results from the technique (7), indicate the outer layer affects on the velocity are reasonably well described but that the footprint of the estimates is not as large as desired, pointing to the need for alternative methods of estimating roughness.

[58] The alternative used here is fitting observed turning of outer boundary layer currents to results from the SLTC model. Because this technique uses measurements from deeper in the boundary layer, it is expected to have larger upstream fetch than techniques that rely on near-interface measurements. Calculations that would quantify the upstream footprint of this technique would be of interest. Another advantage of the velocity profile technique is that it is not limited by restrictive theoretical assumptions because it is based on a detailed numerical boundary layer model. The technique requires profiles of density and currents through the boundary layer, but with recent advances in ice-based observing system technologies, data sets meeting these requirements are becoming more widely available with currently deployed AOFBs in the Arctic.

[59] A comparison of the two methods as applied to the buoy 4 data set is consistent with the idea that the velocity profile technique has a larger footprint than stress technique.

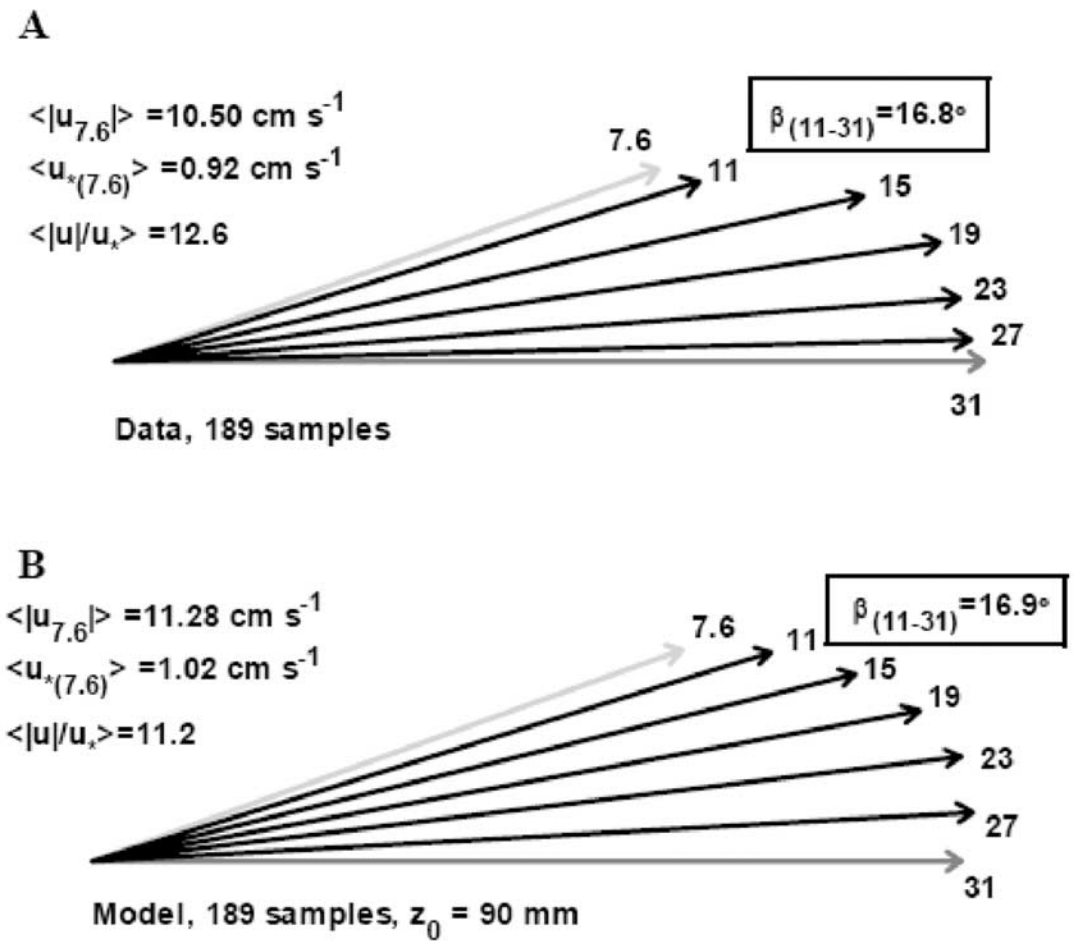


**Figure 12.** Comparison of (a) observed and (b) modeled nondimensional hodographs (with respect to the current vector at 31 m), for all samples with relative current speed at 20 m greater than 0.1 m $s^{-1}$, excluding samples for quadrant I of the traveltime current meter. Listed values refer to the mean values for all samples of speed and friction speed at 7.6 m.

The stress-based $z_0$ estimates are larger than the velocity profile estimates in directions that include the flow disturbance of pressure ridge keels because the smaller fetch of the stress technique is more dominated by the disturbance than the velocity profile technique. For flows in the disturbed quadrants, it is likely that the flux package measurement depth was within the wake of the ice ridge keels, which would result in complications not considered in the extended law of the wall. Nevertheless, averaged over all directions, both techniques yield $z_0$ estimates of about 100 mm. This value is large in comparison with previous roughness estimates which typically range from 5 mm $< z_0 <$ 30 mm [*McPhee et al.*, 2003] and reflects the fact that the earlier estimates were representative of relatively smooth ice and not affected by pressure ridge keels.

[60] Results suggest that both of the techniques are suitable for estimating roughness length. The velocity-profile-based technique is preferred for the IOBL because its larger fetch can produce more spatially representative roughness length estimates. As the AOFB program continues with additional deployments to the Arctic Pack ice, we will continue to compare these techniques and we will construct a record of the variability of roughness estimates that are calculated. The difference between the buoy 3 and buoy 4 stress-based, direction-averaged $z_0$ estimates, 5 mm and 150 mm, is suggestive of variability that we will explore further as more data sets suitable for application of the velocity profile technique are collected.

[61] **Acknowledgments.** Jim Stockel, Rob Wyland, Ron Cowen, and Keith Wyckoff all made significant contributions to the development and construction of the flux buoys. Jamie Morison, Andy Heiberg, and Dean Stewart contributed logistical support and assisted with the field deployment of the buoys at the NPEO camps. This work was supported by NSF grants OPP-0084858 and ARC-0520328. The paper also benefited from the suggestions of two anonymous reviewers.

## References

Blackadar, A. K., and H. Tennekes (1968), Asymptotic similarity in neutral barotropic planetary boundary layers, *J. Atmos. Sci*, *25*, 1015–1020.

Coleman, G. N. (1999), Similarity statistics from a direct numerical simulation of the neutrally stratified planetary boundary layer, *J. Atmos. Sci.*, *56*, 891–900.

Hibler, W. D. (1979), A dynamic thermodynamic sea ice model, *J. Phys. Oceanogr.*, *9*, 815–846.

Horst, T. W., and J. C. Weil (1992), Footprint estimation for scalar flux measurements in the atmospheric surface-layer, *Boundary Layer Meteorol.*, *59*, 279–296.

Jimenez, J. (2004), Turbulent flows over rough walls, *Annu. Rev. Fluid Mech.*, *36*, 173–196.

Krishfield, R. A., and D. K. Perovich (2005), Spatial and temporal variability of oceanic heat flux to the Arctic ice pack, *J. Geophys. Res.*, *110*, C07021, doi:10.1029/2004JC002293.

McPhee, M. G. (1979), The effect of the oceanic boundary layer on the mean drift of pack ice: Application of a simple model, *J. Phys. Oceanogr.*, *9*, 388–400.

McPhee, M. G. (1981), An analytic similarity theory for the planetary boundary layer stabilized by surface buoyancy, *Boundary Layer Meteorol.*, *21*, 325–339.

McPhee, M. G. (1990), Small scale processes, in *Polar Oceanography*, edited by W. Smith, pp. 287–334, Academic, San Diego, Calif.

McPhee, M. G. (1994), On the turbulent mixing length in the oceanic boundary-layer, *J. Phys. Oceanogr.*, *24*, 2014–2031.

McPhee, M. G. (1999), Parameterization of mixing in the ocean boundary layer, *J. Mar. Syst.*, *21*, 55–65.

McPhee, M. G. (2002), Turbulent stress at the ice/ocean interface and bottom surface hydraulic roughness during the sheba drift, *J. Geophys. Res.*, *107*(C10), 8037, doi:10.1029/2000JC000633.

McPhee, M. G. (2008), Physics of early summer ice/ocean exchanges in the western Weddell Sea during ISPOL, *Deep Sea Res., Part II*, *55*, 1075–1097.

McPhee, M. G., T. Kikuchi, J. H. Morison, and T. P. Stanton (2003), Ocean-to-ice heat flux at the North Pole environmental observatory, *Geophys. Res. Lett.*, *30*(24), 2274, doi:10.1029/2003GL018580.

Notz, D., M. G. McPhee, M. G. Worster, G. A. Maykut, K. H. Schlunzen, and H. Eicken (2003), Impact of underwater-ice evolution on arctic summer sea ice, *J. Geophys. Res.*, *108*(C7), 3223, doi:10.1029/2001JC001173.

Skyllingstad, E. D., C. A. Paulson, W. S. Pegau, M. G. McPhee, and T. Stanton (2003), Effects of keels on ice bottom turbulence exchange, *J. Geophys. Res.*, *108*(C12), 3372, doi:10.1029/2002JC001488.

Tennekes, H., and J. L. Lumley (1972), *A First Course in Turbulence*, MIT Press, Cambridge, Mass.

Wadhams, P. (1988), The underside of arctic sea ice imaged by sidescan sonar, *Nature*, *333*, 161–164.

Wadhams, P., J. P. Wilkinson, and S. D. McPhail (2006), A new view of the underside of Arctic Sea ice, *Geophys. Res. Lett.*, *33*, L04501, doi:10.1029/2005GL025131.

T. Kikuchi, Japan Marine Science and Technology Center, Yokosuka 237-0061, Japan. (takashik@jamstec.go.jp)

M. G. McPhee, McPhee Research Company, Naches, WA 98937, USA. (mmcphee@starband.net)

W. J. Shaw and T. P. Stanton, Oceanography Department, Naval Postgraduate School, Monterey, CA 93943, USA. (wjshaw@nps.edu; stanton@nps.edu)